Journal of
Materials Chemistry C

ROYAL SOCIETY
OF CHEMISTRY

PAPER

View Article Online
View Journal | View Issue

Cite this: *J. Mater. Chem. C*, 2026, **14**, 6277

Investigating the effects of planarized *versus* twisted donors on a multiple resonance thermally activated delayed fluorescence core

Mitchell J. Demchuk, Ryoga Hojo, Changfeng Si and Zachary M. Hudson*

Received 13th December 2025,
Accepted 8th February 2026

DOI: 10.1039/d5tc04366b

rsc.li/materials-c

Multiple resonance thermally activated delayed fluorescence (MR-TADF) emitters are known for their short-range charge transfer excited states and rigid, planar π-frameworks. In contrast, donor–acceptor TADF materials are typically dominated by long-range charge transfer excited states and twisted π-frameworks. An emerging design strategy that seeks to combine these two approaches can be achieved by appending a donor moiety to an MR-TADF core. This strategy has been shown to enhance desirable photophysical properties, such as increasing the rate of reverse intersystem crossing, due to spin-vibronic coupling between excited states of differing orbital symmetry. Here, two donor-appended materials based on the BNCz MR-TADF core are investigated using the donors HMAT (hexamethylazatriangulene) and ACR (9,9-dimethyl-9,10-dihydroacridine). Though structurally similar, the HMAT donor is a fused π-skeleton that provides a higher degree of planarity. In contrast, the ACR donor remains unfused and adopts a twisted structure. This difference leads to altered solution-state photophysical properties which are further investigated using a Lippert–Mataga analysis and theoretical calculations. Solid-state measurements of both emitters, **HMAT-BNCz** and **ACR-BNCz**, are then performed to elucidate the impact of donor rigidity on their TADF properties.

Introduction

Thermally activated delayed fluorescence (TADF) materials have undergone substantial development over the past decade, in particular for application in organic light emitting diodes (OLEDs).[1–7] OLEDs are leading the field of display technology owing to their fast response time, high contrast ratio, and thin form factors.[6,8] TADF materials provide several advantages over other classes of materials that can be used as emitters in OLEDs, namely that they can utilize both singlet and triplet excitons for radiative processes through reverse intersystem crossing (rISC), without the need for rare metal elements.[2,9,10] Since singlet and triplet excitons are formed in a ratio of 1 : 3 in electroluminescent devices, organic TADF materials can theoretically achieve 100% internal quantum efficiencies in fully organic systems.[1,10–12] There is however still potential to improve these materials in terms of their external quantum efficiencies, and the availability of stable, pure blue TADF emitters at display-relevant chromaticities. Therefore, the development and testing of various design strategies for TADF emitters is critical to full scale industrial implementation.[13]

In terms of molecular design, TADF is achieved by minimizing the energy gap between the lowest excited singlet (S_1) and triplet (T_1) excited states, termed ΔE_{ST}. This is achieved through spatial separation of the highest occupied molecular orbital (HOMO) and lowest unoccupied molecular orbital (LUMO), correlating to a decrease in the electron exchange energy that separates the S_1 and T_1 energy levels.[1,10] A $\Delta E_{ST} < 0.3$ eV generally allows for appreciable rISC rates, resulting in delayed fluorescence. To achieve this, donor–acceptor frameworks can be utilized, where the HOMO and LUMO are localized on the donor and acceptor moieties, respectively.[1,11,14,15] Imposing a large torsion angle between the donor and acceptor moieties ensures sufficient separation of the HOMO and LUMO, inducing TADF character.[15,16] However, their usefulness in OLEDs is challenged by the inherently broad emission spectra produced by compounds with long-range charge transfer (LRCT), leading to low colour purity.

To address this problem, Hatakeyama and coworkers developed multiple-resonance TADF (MR-TADF) which incorporates a donor atom (*e.g.* nitrogen) and acceptor atom (*e.g.* boron) in a rigid, polycyclic aromatic framework.[17] This design allows the HOMO and LUMO to become atomically localized in an alternating fashion, which minimizes molecular vibrations to provide narrowband emission.[2,3,17–19] When incorporated into OLEDs, these features provide high colour purity, high device

---

Department of Chemistry, The University of British Columbia, 2036 Main Mall, Vancouver, British Columbia, V6T 1Z1, Canada. E-mail: zhudson@chem.ubc.ca; Fax: +1-604-822-2847; Tel: +1-604-822-3266

efficiencies, and improved stability, enhancing overall device performance. Recent work has largely focused on extending the π-conjugation of these materials or increasing spin–orbit coupling (SOC) by introducing heavy atoms such as sulfur, selenium and bromine.[14,20,21]

Another promising strategy to enhance photophysical properties and tune emission colour is through appending donor moieties to MR-TADF cores.[22–24] One of the most important advantages of this strategy is that appended donors can introduce LRCT character to these systems – which can in turn increase the rate constant for rISC (k_{rISC}) by altering the excited state character of S_1 and T_1.[20,25–28] In the case of BNCz, this can be achieved through fusing an electron-donating unit para- to the boron atom, introducing a LRCT triplet excited state to the material.[25,26,29] This then facilitates the forbidden transition between triplet and singlet SRCT states in the MR-TADF core through a higher-order spin-vibronic mechanism, enhancing the rate of rISC.[3,25,30] The drawback of this approach is that if too much LRCT character is introduced, it can lead to spectral broadening and lower photoluminescent quantum yields (PLQYs).

The MR-TADF emitter BNCz (alternatively known as DtBuCzN) has received much attention since its discovery in 2020 by Wang, Zhang and coworkers.[31] The polycyclic aromatic core is based on the fusion of two di-*tert*-butyl carbazole moieties with a central boron atom (Scheme 1). The BNCz motif has many attractive properties, including a narrow emission spectrum ($\lambda_{\max}$ = 481 nm, FWHM = 22 nm), low ΔE_{ST} (0.13 eV), and high PLQY (91% in toluene).[31] The ease of synthesizing and modifying this molecule has also proven advantageous, allowing many groups to tune its structure to achieve desired properties. For example, Zhao, Huo and coworkers recently reported BNCz modified with triphenylamine donors appended to the central benzene ring *para* to boron, which resulted in accelerated rISC and aggregation-induced emission enhancement (Scheme 1).[26] This can be attributed to an increase of the charge transfer character of high-lying triplet excited states in BNCz, facilitated by the donor moieties. In 2020, Wang *et al.* synthesized **m-Cz-BNCz**, which has a carbazole donor attached to the *meta* position of the benzene rings with respect to boron (Scheme 1).[27] **m-Cz-BNCz** was significantly red-shifted compared to BNCz and showed narrowband green emission. A large torsion angle between the donor and BNCz core promoted combined LRCT and MR-TADF properties. The authors also found that the HOMO energy of **m-Cz-BNCz** was significantly increased compared to BNCz alone.[27] This can be attributed to the fact that the central benzene ring in BNCz has the LUMO localized at the *para* position, while the HOMO is localized at the *meta* positions. Thus, di-*tert*-butylcarbazole appended to the *meta* position can influence the frontier molecular orbitals of the BNCz core.

Another prominent example of donor-functionalized MR-TADF cores comes from Yang, Cao and coworkers in 2023, where they attached a phenoxazine donor on the central benzene ring of BNCz, *para* to the boron atom (Scheme 1).[25] The authors demonstrated that appending a phenoxazine donor to BNCz can boost rISC rates, while alteration of the electronic/steric properties in this molecule leads to emission from excited states of varying character (SRCT, LRCT or a hybrid SRCT/LRCT state).[25] Many more strategies for tuning the properties of BNCz have been exploited, such as appending acceptor moieties, incorporating donors positioned for through-space charge transfer, and improving π-conjugation and molecular orbital delocalization.[18,26,32–35]

Herein, we describe two donor-appended MR-TADF molecules using BNCz as the core and either HMAT (hexamethylazatriangulene) or ACR (9,9-dimethyl-9,10-dihydroacridine) as donors on the central benzene ring *para* to boron. (Scheme 1).

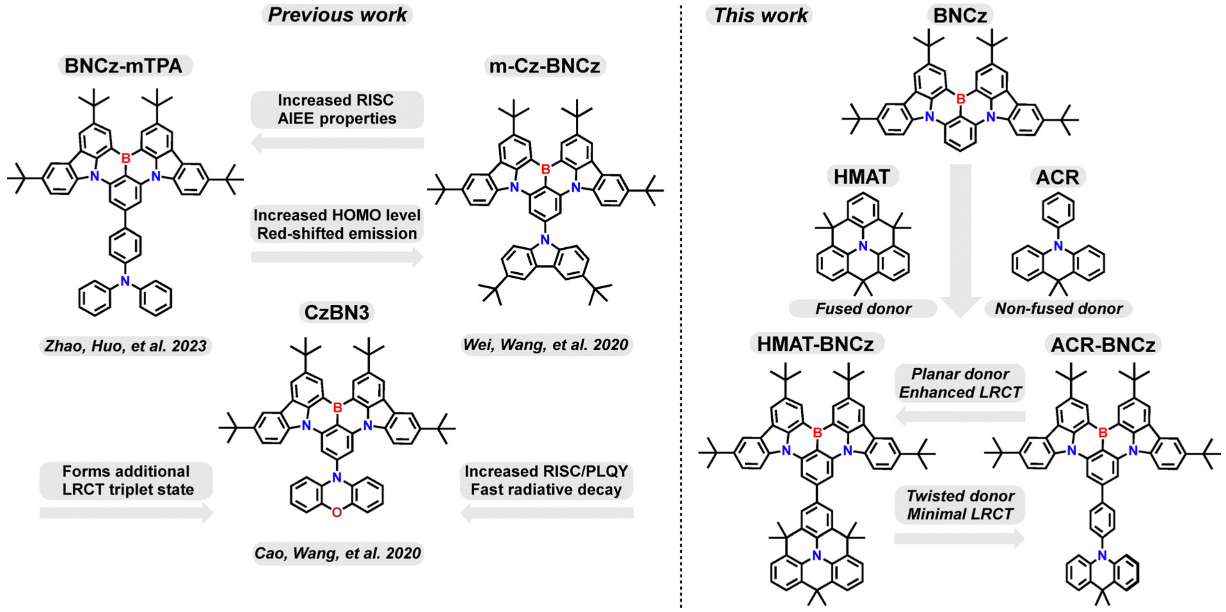

Scheme 1 Left: Previously reported BNCz donor appended systems and their properties. Right: This work, exploring the difference between similar donors when planarized *versus* twisted in BNCz MR-TADF systems.

Our group has previously reported the use of HMAT and ACR donors in donor–acceptor TADF emitters, which have applications in OLED design, biological imaging, and energy transfer photocatalysis.[36–41] We were interested to explore how the photophysical properties of the ACR donor linked to BNCz through a phenyl spacer would differ from that of the planar HMAT donor, which is fused to the phenyl spacer with dimethylmethylene groups. This fused structure encourages increased conjugation between HMAT and the MR-TADF core, while the unfused ACR donor remains twisted with respect to the BNCz unit (Scheme 1). We find that **HMAT-BNCz** and **ACR-BNCz** both have slightly red-shifted emission spectra with similar FWHM values when compared to BNCz. Additionally, while **ACR-BNCz** retains a PLQY of 91% in degassed toluene (identical to BNCz), the PLQY of **HMAT-BNCz** is somewhat lower at 80%. Notably, the solution photophysics of **HMAT-BNCz** indicates significant LRCT character, whereas **ACR-BNCz** retains MR-type SRCT character. A Lippert–Mataga analysis in concert with theoretical calculations point to emission from an alternative, LRCT excited state when stabilized in polar solvents for **HMAT-BNCz**, but not in **ACR-BNCz**. Finally, solid state measurements of both emitters doped into a 1 wt% PMMA film confirm their TADF nature, with delayed lifetimes of 96.8 µs and 101.9 µs for **HMAT-BNCz** and **ACR-BNCz**, respectively. Overall, this work showcases how structurally similar donors can influence the photophysical properties of the MR-TADF emitter BNCz, by adopting either a planar or twisted orientation, facilitated by ring fusion.

Results and discussion

HMAT-BNCz and **ACR-BNCz** were synthesized through a Suzuki–Miyaura cross coupling reaction between BNCz-bromide and pinacolboranes of HMAT or ACR, respectively. BNCz-Br, as well as HMAT-BPin and ACR-BPin were prepared as per literature reports.[35,42,43] Both reactions occur in good yield, 79% for **HMAT-BNCz** and 88% for **ACR-BNCz** (Fig. S1–S8). Single crystals of both emitters were obtained through slow evaporation from hexanes at room temperature and single crystal X-ray diffraction was used to obtain their solid-state structures. The main structural difference between in these two emitters is the torsion angle between the MR-TADF core and the donor group. In **ACR-BNCz**, the benzene ring linking ACR to the core is approximately planar, suggesting it is in conjugation with the BNCz moiety (torsion angle ∼18°). The torsion angle between the BNCz core and the acridine donor is significantly more twisted at ∼86° (Fig. 1). In contrast, for **HMAT-BNCz** the benzene ring linked to the MR-TADF core is fused by two dimethylmethylene groups, which locks it in a more planar configuration with a torsion angle of ∼19° between the HMAT donor and the BNCz core (Fig. 1).

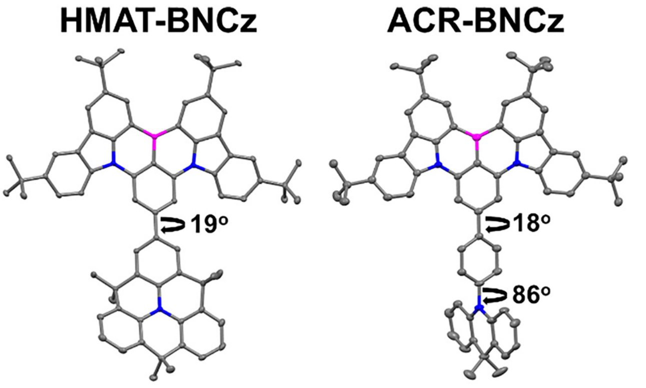

Fig. 1 Solid-state structures of **HMAT-BNCz** and **ACR-BNCz** showing torsion angles between donors and MR-core. Hydrogen atoms have been omitted for clarity; thermal ellipsoids are depicted at 50% probability level. Grey: carbon, blue: nitrogen, magenta: boron.

In the ultraviolet-visible (UV-Vis) absorption spectrum, **HMAT-BNCz** has a λ_{max} = 471 nm ($\varepsilon = 8.03 \times 10^4\ cm^{-1}\ M^{-1}$) and **ACR-BNCz** has a similar λ_{max} = 470 nm ($\varepsilon = 6.22 \times 10^4\ cm^{-1}\ M^{-1}$) (Fig. 2a and b). Though the λ_{max} values are nearly identical, **HMAT-BNCz** has an additional large charge-transfer band from 375–430 nm, whereas **ACR-BNCz** has none. The PL spectra in a 10 µM toluene solution showed a λ_{max} = 489 nm for **HMAT-BNCz** and λ_{max} = 491 nm for **ACR-BNCz**, with narrow full width at half maximum (FWHM) of 22 nm and 24 nm, and small Stokes shifts of 18 nm and 21 nm, respectively. Both emitters showed evidence of positive solvatochromism, with hexanes showing the greatest blue shift and acetonitrile the greatest red shift (Fig. 2c and d). Supporting the hypothesis that HMAT induces more CT character

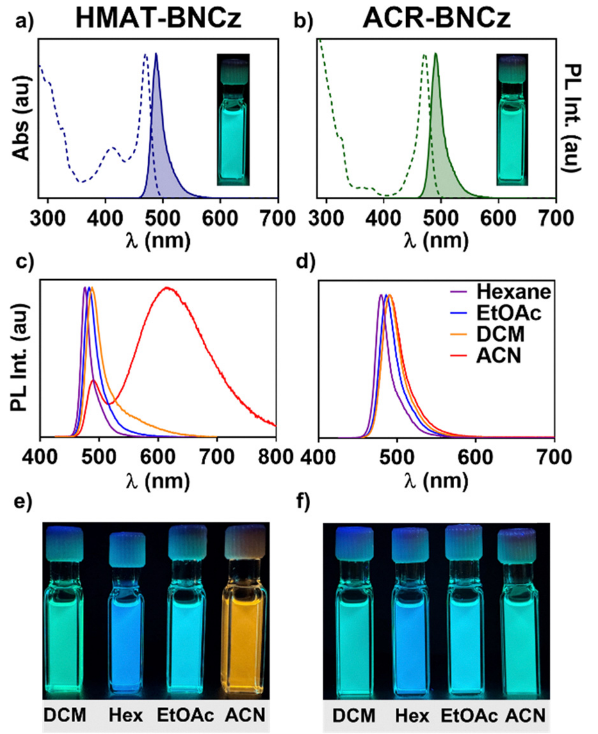

Fig. 2 Normalized UV-Visible absorption and steady-state PL spectra of **HMAT-BNCz** (a) and **ACR-BNCz** (b) in toluene. Normalized PL spectra of **HMAT-BNCz** (c) and **ACR-BNCz** (d) in varying solvents. Photographs of **HMAT-BNCz** (e) and **ACR-BNCz** (f) in various solvents. All spectra were measured at a concentration of 10 µM. Emission spectra were excited at 375 nm.

than ACR, when **HMAT-BNCz** is placed in a 10 μM acetonitrile solution, its colour shifts to bright orange (Fig. 2e) and exhibits dual emission, with a new broad charge transfer (FWHM = 140 nm) at λ_{max} = 615 nm, in addition to a narrow SRCT band at 494 nm. This is significantly different from the nature of **ACR-BNCz** in a 10 μM acetonitrile solution, which stays a blue/green in colour and has a λ_{max} = 490 nm, indicative of SRCT type emission (Fig. 2f).

We then conducted a Lippert–Mataga analysis to further investigate the photophysical response of each emitter to solvent polarity, by examining the relationship between Stokes shift ($\nu_a - \nu_f$) and solvent orientational polarizability (Δf). The Lippert–Mataga equation (eqn (S1)) can then be used to determine the molecule's excited-state dipole moment (μ_e).[44] The excited-state dipole moment value is known to be larger for LRCT-type emitters, when compared to emitters whose luminescence originates from locally excited or SRCT states.[25,44,45] **HMAT-BNCz** exhibits dual emission upon dissolution in the four most polar solvents tested, one with narrowband SRCT character and one with a broad,-redshifted emission peak showing LRCT character (Fig. 3). We predict this is most likely caused by stabilization of a low-lying S_2 state which exhibits LRCT, due to the fused, planar HMAT donor. This is in contrast to **ACR-BNCz**, an unfused, twisted donor exhibiting only SRCT emission character even in the most polar solvents. The **HMAT-BNCz** emitter was found to have two excited-state dipole moments (μ_e) of 7.4 D and 39.5 D (D = Debye), while **ACR-BNCz** shows only one μ_e of 6.9 D (Fig. 3) (μ_e values calculated using eqn (S1)–(S4) and Table S1). The first μ_e of **HMAT-BNCz** and only μ_e of **ACR-BNCz** are smaller values, as expected of the narrowband SRCT emission originating from the MR-TADF core. The larger μ_e of 39.5 D for **HMAT-BNCz** corresponds to a new red-shifted broad emission band in more-polar solvents and can most likely be attributed to additional LRCT character induced by the HMAT donor on the BNCz core (see DFT analysis below).

Subsequently, phosphorimetry studies were performed in a 10 μM 2-MeTHF glass at 77 K. The experimentally determined S_1, T_1 and ΔE_{ST} values were calculated by the onset of fluorescent and phosphorescent emission through obtaining steady-state and time-gated spectra (Fig. S11). **HMAT-BNCz** shows S_1 and T_1 energies of 2.65 eV and 2.48 eV respectively, giving a ΔE_{ST} = 0.17 eV. For **ACR-BNCz**, the S_1 and T_1 energies lie at 2.64 eV and 2.48 eV, giving a ΔE_{ST} = 0.16 eV. These ΔE_{ST} values are slightly larger compared to that of the parent BNCz compound, which has a ΔE_{ST} of 0.13 eV, yet are still well within range to showcase TADF behavior. In a 10 μM toluene solution, the PLQY of **HMAT-BNCz** was 80% (under N_2) and 59% (in air), while the values for **ACR-BNCz** were slightly higher at 91% (under N_2) and 66% (in air). PL decays in a toluene solution were measured using time correlated single-photon counting (TCSPC), while the delayed fluorescence component was monitored using multi-channel scaling (MCS). We found that **HMAT-BNCz** had a prompt lifetime of 5.14 ns (inert) and 4.48 ns (air), while **ACR-BNCz** had a prompt lifetime of 5.38 ns (inert) and 4.68 ns (air) (Fig. S13). The delayed fluorescence components were found to be 4.7 μs for **HMAT-BNCz** and 3.1 μs for **ACR-BNCz** under inert conditions (Fig. S14). Table 1 summarizes the solution state photophysics for each compound. Intrigued by the fact that **HMAT-BNCz** shows dual emission with a broad CT band while the more twisted and flexible **ACR-BNCz** does not, fluorescence lifetime measurements for each emitter were obtained in 10 μM acetonitrile solutions (Fig. S15 and S16). Under inert conditions the prompt fluorescence lifetimes for **HMAT-BNCz** were found to be 11.4 ns (at λ_{max} = 615 nm) and 10.9 ns (at λ_{max} = 494 nm), while **ACR-BNCz** has a prompt lifetime of 9.4 ns in acetonitrile. Interestingly, **HMAT-BNCz** was found to have a completely quenched delayed lifetime in acetonitrile (identical PL decay curves under nitrogen vs air) for both λ_{max} = 615 nm and λ_{max} = 494 nm emission bands, while **ACR-BNCz** retained a delayed fluorescence lifetime of 7.8 μs under nitrogen, while quenched in air.

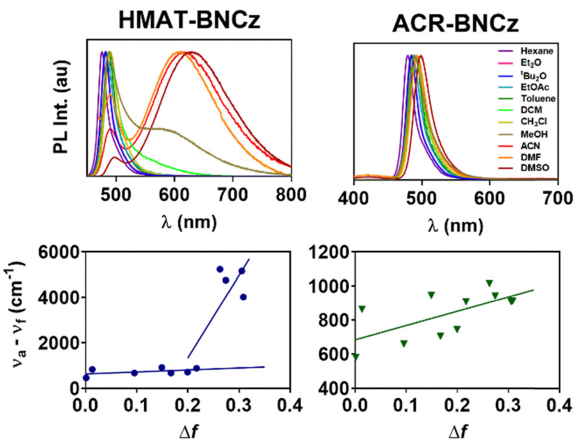

Fig. 3 Normalized photoluminescent spectra of **HMAT-BNCz** and **ACR-BNCz** taken in each solvent as a 10 μM solution (top). Lippert–Mataga plots of **HMAT-BNCz** and **ACR-BNCz** (bottom).

The solid state photophysical properties of these emitters were then investigated by doping them into a poly(methyl methacrylate) (PMMA) film using 1 wt% emitter. Both emitters showcased a blue-shifted emission in the solid state, with λ_{max} at 486 nm for **HMAT-BNCz** and 485 nm for **ACR-BNCz** (Fig. S17). The PLQY of both compounds in the PMMA film were measured to be lower than in solution, with **HMAT-BNCz** Φ_{PL} = 21.6% and **ACR-BNCz** Φ_{PL} = 20.2%. The prompt fluorescence lifetime for **HMAT-BNCz** remained unchanged from the solution state under inert conditions at 5.1 ns, while **ACR-BNCz** showed a slight increase to τ_p^{Ar} = 6.1 ns (Fig. S20). At 298 K, both emitters showed a delayed component, with **HMAT-BNCz** having a shorter delayed lifetime of 96.8 μs, and **ACR-BNCz** with a slightly longer delayed lifetime of 101.9 μs. Upon cooling from 298 K to 100 K, suppression of the delayed lifetime is observed confirming TADF character (Fig. 4). Summarized solid-state emission and lifetime data for 1 wt% doped PMMA films can be found in Table S2. Emission spectra and lifetime measurements for **HMAT-BNCz** and **ACR-BNCz** were also collected for 1 wt% doped Zeonex films to assess if there would be any change in photophysical properties within a less polar thin film. The emission spectra slightly blueshifts for

Table 1 Photophysical data in toluene solution

Entry	λ_{abs} (nm) ε (10^4 cm^{-1} M^{-1})	$\lambda_{max,em}$ (nm)	FWHM (nm)	Φ_{air}/Φ_{N2}	CIE (x,y)	τ_p^{air} (ns)	τ_p^{N2} (ns)	τ_d^{N2} (us)
HMAT-BNCz	470 (6.2)	489	22	0.59/0.80	(0.085, 0.384)	4.5	5.1	4.7
ACR-BNCz	471 (8.0)	491	24	0.66/0.91	(0.083, 0.423)	4.7	5.4	3.1

All measurements were performed in 10 μM toluene solutions (λ_{ex} = 375 nm). Absolute photoluminescence quantum yields were determined using an integrating sphere.

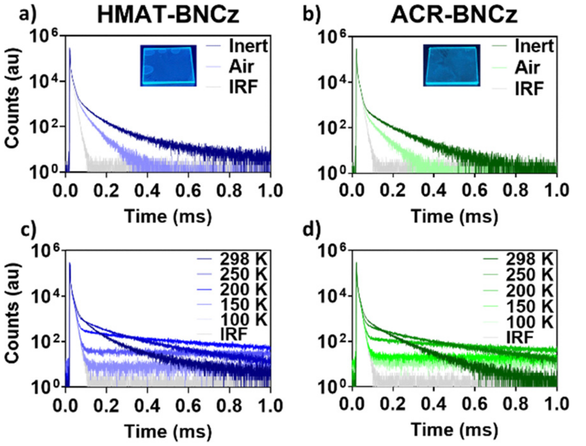

Fig. 4 PL decays under air *versus* argon at 298 K of **HMAT-BNCz** (a) and **ACR-BNCz** (b). PL decays at various temperatures between 100 K and 298 K for **HMAT-BNCz** (c) and **ACR-BNCz** (d). Measurements taken as 1 wt% doped PMMA films. λ_{exc} = 375 nm for **HMAT-BNCz** and λ_{exc} = 300 nm for **ACR-BNCz**.

HMAT-BNCz with λ_{max} = 481 nm, while **ACR-BNCz** emission remains nearly unchanged at λ_{max} = 486 nm. Under inert conditions, **HMAT-BNCz** shows a τ_d^{Ar} = 111.1 μs and a τ_p^{Ar} = 5.0 ns, while **ACR-BNCz** shows a τ_d^{Ar} = 91.9 μs and a τ_p^{Ar} = 7.3 ns. Overall, doping these emitters into PMMA *versus* Zeonex films was found to have little effect on their photophysical properties in the solid state (Fig. S21–S23 and Table S3). We then tested the emitters doped into a 1 wt% film of the OLED host material 1,3-bis(*N*-carbazolyl)benzene (mCP). Both **HMAT-BNCz** and **ACR-BNCz** exhibit a redshift compared to their PMMA and Zeonex film counterparts, with an λ_{max} = 496 nm and 497 nm, respectively. Under inert conditions, **HMAT-BNCz** shows a τ_d^{Ar} = 71.4 μs and a τ_p^{Ar} = 5.5 ns, while **ACR-BNCz** shows a τ_d^{Ar} = 80.9 μs and a τ_p^{Ar} = 5.4 ns. Overall, the mCP host induces a significant redshift in both emitters and a shortened delayed lifetime in the solid state (Fig. S24–S26 and Table S4).

Photostability studies were then conducted on toluene solutions of both compounds to gauge their relative stabilities, using both 365 nm and 450 nm LED irradiation (ensuring both compounds had the same initial absorbance values at each excitation wavelength). UV-Vis absorption and PL spectra were taken at varying time intervals until decomposition was observed. Under 365 nm irradiation, **HMAT-BNCz** decomposed faster compared to **ACR-BNCz** over the course of 360 minutes (Fig. S27 and S28). Under these conditions it was determined that **ACR-BNCz** is approximately 35% more stable than **HMAT-BNCz** when comparing the decomposition slopes of UV-Vis spectra. Under 450 nm irradiation both compounds degraded significantly faster over 150 minutes (Fig. S29 and S30).

HOMO and LUMO energies were determined experimentally using cyclic voltammetry in a degassed DCM solution. **HMAT-BNCz** shows two reversible one-electron oxidations and one irreversible reduction, while **ACR-BNCz** shows two quasi-reversible one electron oxidations and one irreversible reduction (Fig. S31). From the oxidation and reduction potentials (referenced to ferrocene/ferrocenium, $Fc^{0/+}$), HOMO/LUMO values of −5.27/−2.63 eV for **HMAT-BNCz** (E_{gap} = 2.57 eV) and −5.41/−2.57 eV for **ACR-BNCz** (E_{gap} = 2.56 eV) were obtained (Table S5). When compared to the parent MR-TADF material BNCz (HOMO = −5.40 eV, LUMO = 3.35 eV and E_{gap} = 3.35 eV) both emitters have a lower LUMO level. However, the planar HMAT donor induces a significantly higher HOMO level, while the twisted ACR donor HOMO level is nearly identical.

Theoretical calculations

Density functional theory (DFT) calculations were performed to further investigate the electronic and photophysical properties of both emitters. Geometry optimizations were performed at the TPSSh/def2SVP level, followed by use of the Tamm–Dancoff approximation (TDA) for time-dependent DFT calculations at the RI-B2PLYP/def2-TZVP/CPCM(toluene) level of theory. TDA-DFT was used for excited state theoretical calculations, as it has proved suitable for large molecules which may suffer from triplet instability problems.[46] In general, the results yielded by DFT match well with trends seen in experimental data. For **HMAT-BNCz**, the calculated S_1/T_1 values were 2.75 eV and 2.65 eV, respectively, with a ΔE_{ST} value of 0.10 eV. For **ACR-BNCz**, the theoretically calculated S_1/T_1 values were 2.74 eV and 2.61 eV, respectively, with a ΔE_{ST} value of 0.13 eV. Both emitters predicted ΔE_{ST} values are slightly lower than their experimentally determined values (less than 0.07 eV for each). To support the experimentally observed trends in fluorescent lifetime data and Lippert–Mataga analysis, excited state singlet energies were calculated at the RI-B2PLYP/def2-TZVP/CPCM(toluene) level of theory. **HMAT-BNCz** has a calculated S_1 = 2.75 eV and S_2 = 2.96 eV ($\Delta S_1/S_2$ = 0.21 eV), while **ACR-BNCz** has a calculated S_1 = 2.74 eV and S_2 = 3.11 eV ($\Delta S_1/S_2$ = 0.37 eV). Additionally, electron–hole diagrams were generated at the RI-B2PLYP/def2-TZVP/CPCM(toluene) level of theory.

As seen in Fig. 5, the S_1 state for both **HMAT-BNCz** and **ACR-BNCz** is dominated by MR-type SRCT character, with the electron and hole distributions localized on alternating atoms of the BNCz-core. Considering the electron–hole distribution

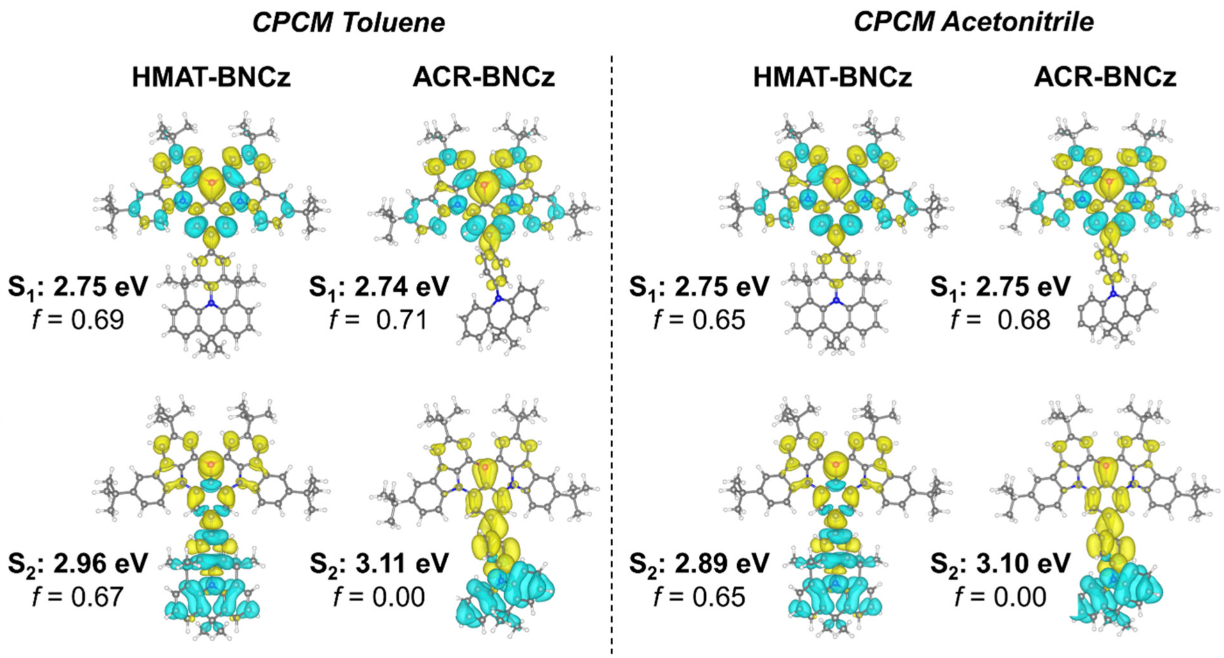

Fig. 5 Hole–electron (blue-yellow) diagrams and oscillator strengths were calculated using TDA-TDDFT at the RI-B2PLYP/def2-TZVP level of theory using CPCM(toluene) and CPCM(acetonitrile).

for the S_2 state, both molecules show more prominent LRCT character, like that of D/A TADF compounds. Using these theoretical predictions, we can determine that in polar solvents, the S_2 excited state of **HMAT-BNCz** is likely stabilized to an energy lower than or close to the original S_1 state, resulting in the observed LRCT emission. To further validate this theory, the oscillator strength (f) for **HMAT-BNCz** was calculated to be 0.69 for the $S_0 \rightarrow S_1$ transition and 0.67 for the $S_0 \rightarrow S_2$ transition. The oscillator strength of **ACR-BNCz** for the $S_0 \rightarrow S_1$ transition was calculated to be 0.71, and zero for the $S_0 \rightarrow S_2$ transition (Table S6). This information allows us to deduce that emission from the S_2 state is much more likely in **HMAT-BNCz** than **ACR-BNCz** due to its significantly greater f ($S_0 \rightarrow S_2$) and smaller S_1/S_2 energy gap, supporting experimental observations in the Lippert–Mataga analysis. The SOC values between $S_0/S_1/S_2$ and T_1/T_2 were calculated at the TPSSH def2-TZVP level of theory in toluene using a conductor-like polarizable continuum (CPCM). The SOC between S_1/T_1 were found to be moderately larger for **HMAT-BNCz** at 0.17 cm^{-1}, when compared to **ACR-BNCz**, with a very small value of 0.03 cm^{-1} (Table S7). This can likely be attributed to the greater difference in nature of orbital types introduced by the planar HMAT donor, when compared to the twisted ACR donor. Finally, to confirm the S_1 and S_2 excited state character, a percent charge transfer analysis was performed for both emitters at the RI-B2PLYP/def2-TZVP/CPCM(toluene) level of theory, using the interfragment charge transfer method (Table S8). For **HMAT-BNCz,** the S_1 state has 95.2% SRCT and 4.8% LRCT character, while the S_2 state has 38.1% SRCT and 61.9% LRCT character. For **ACR-BNCz** the S_1 state was found to have 94.7% SRCT and 5.3% LRCT character, while the S_2 state shows 46.9% SRCT and 53.1% LRCT character.

To further lend support to these findings, excited state calculations were repeated using the solvent acetonitrile within the CPCM model instead of toluene, at the RI-B2PLYP/def2-TZVP/CPCM(acetonitrile) level of theory. Calculations revealed **HMAT-BNCz** and **ACR-BNCz** ΔE_{ST} values of 0.12 eV and 0.14 eV, respectively, both less than 0.02 eV greater than those calculated in toluene. Importantly, calculations using acetonitrile show that **HMAT-BNCz** has an S_1 = 2.75 eV and S_2 = 2.89 eV ($\Delta S_1/S_2$ = 0.14 eV), where the S_1 energy does not change *versus* the theoretical calculations in toluene, but the S_2 energy is stabilized by 0.07 eV. For **ACR-BNCz**, the S_1/S_2 values were changed by only 0.01 eV each with no change in $\Delta S_1/S_2$. Calculated oscillator strengths in acetonitrile were found to be 0.65 for both the $S_0 \rightarrow S_1$ and $S_0 \rightarrow S_2$ transition in **HMAT-BNCz**, while values of 0.68 for the $S_0 \rightarrow S_1$ transition and zero for the $S_0 \rightarrow S_2$ transition were calculated for **ACR-BNCz**, consistent with experimental observations (see Tables S9–S11 for summarized theoretical data using CPCM(acetonitrile) and percent charge transfer analysis). Finally, electron–hole diagrams were generated at the RI-B2PLYP/def2-TZVP/CPCM(acetonitrile) level of theory (Fig. 5). Similar to the toluene CPCM model, the electron–hole distribution map using acetonitrile depicts an MR-type SRCT character dominated S_1 state and a D/A-type LRCT character dominated S_2 state.

Conclusions

In conclusion, TADF emitters **HMAT-BNCz** and **ACR-BNCz** have been synthesized utilizing the donor appended MR-TADF core design strategy. The fused and planarized nature of the HMAT donor leads to altered photophysical properties in solution when compared to the non-fused and twisted ACR donor. Solid-state measurements confirm the TADF activity of both compounds, with **HMAT-BNCz** having a τ_d^{Ar} = 96.8 µs (ΔE_{ST} = 0.17 eV) and **ACR-BNCz** having a τ_d^{Ar} = 101.9 µs (ΔE_{ST} = 0.16 eV) in 1 wt% PMMA films. Notably, **HMAT-BNCz** shows a large solvatochromic response in high-polarity solvents, leading to dual emission peaks with a significantly red-shifted and broadened emission spectra. This was investigated using a Lippert–Mataga analysis, showing **HMAT-BNCz** has two excited state dipole moments of μ_e = 7.4 D (SRCT character) and μ_e = 39.5 D (LRCT character), while **ACR-BNCz** has only one μ_e = 6.9 D (SRCT character). Theoretical calculations reveal that this difference in emission character is likely due to the S_2 state of **HMAT-BNCz** being stabilized in more polar solvents, leading to dual emission. Although a TICT state cannot be fully ruled out, we believe there is strong evidence for dual emission originating from S_1 and a stabilized S_2 state in polar solvents such as acetonitrile for **HMAT-BNCz** – owing to its fused and planarized structure when compared to **ACR-BNCz**. This is supported by the fact that **HMAT-BNCz** has identical calculated oscillator strengths for both the S_0–S_1 and S_0–S_2 transitions of 0.65, with a small $\Delta S_1/S_2$ in acetonitrile. This study enhances our understanding of how the donor-appended MR-TADF design strategy can be used to alter emission character between MR dominated SRCT and D/A dominated LRCT excited states, by exploring the difference between two structurally similar donors in a planar *versus* twisted geometry.

Experimental details

General considerations

All reactions and material manipulation were carried out under a nitrogen atmosphere using either standard Schlenk line or glovebox techniques unless stated otherwise. Dry and degassed toluene was obtained using an Innovative Technologies Inc. solvent purification system. Ethanol (99%) and deionized water were degassed using nitrogen for 30 minutes prior to use. All reagents were obtained from Sigma-Aldrich, TCI America and Oakwood Chemical, and used as received unless otherwise stated. HMAT-BPin, ACR-BPin and BNCz-Br were prepared according to literature procedures.[35,42,43] High resolution mass spectrometry (HRMS) data were obtained with field desorption (FD+) using a Jeol JMS-T100GCV AccuTOF GCv 4G spectrometer. The ^{1}H and ^{13}C{^{1}H} nuclear magnetic resonance (NMR) spectra were measured on a Bruker AV III HD 400 MHz spectrometer with benzene-d$_6$ (C_6D_6) or dichloromethane-d$_2$ as the solvent.

General photophysical characterization

Absorbance measurements were taken on a Cary 60 spectrometer and fluorescence measurements were performed using an Edinburgh Instruments FS5 spectrofluorometer or Edinburgh Instruments FLS1000 spectrofluorometer. Absolute photoluminescence quantum yields were determined using an Edinburgh Instruments SC–30 Integrating Sphere Module, with optical densities less than 0.1. Lifetimes were obtained using the Edinburgh Instruments FLS1000 spectrofluorometer and an EPLED (λ_{exc} = 375 nm or 300 nm) coupled with time-correlated single-photon counting (TCSPC), or a Xe µF lamp coupled with multichannel scaling (MCS). Concentrations of 10 µM were used unless otherwise stated. All solution state UV-Visible and fluorescence data were obtained using standard quartz cuvettes. Phosphorimetry was performed using a quartz tube and films were prepared on quartz or sapphire slides.

Electrochemical methods

Cyclic voltammograms were measured using BASi Epsilon Eclipse potentiostat at room temperature with a standard cell three-electrode configuration. The working electrode was a 3 mm diameter glassy carbon electrode. The reference electrode was a Ag wire in a 0.2 M tetrabutylammonium hexafluorophosphate ([^{n}Bu$_4$][PF$_6$]) DCM solution, referenced externally to ferrocene/ferrocenium. The counter electrode was a Pt wire. Measurements were performed in a 0.2 M ([^{n}Bu$_4$][PF$_6$]) DCM solution with 1 mM analyte at scan rates of 100 and 200 mV s^{-1}.

Density functional theory

Quantum chemical calculations were conducted using Gaussian 16 with default settings unless otherwise stated. Ground state energies and corresponding geometries were calculated at the TPSSh/def2SVP level of theory. Tamm–Dancoff approximation (TDA) DFT was performed from the optimized frequencies at the B2PLYP/def2-TZVP level of theory using CPCM(toluene) and CPCM(acetonitrile) with ORCA 6.1.0. Electron–hole analysis and was performed using Multiwfn version 3.8 (dev) and visualized in VESTA (Visualization for Electronic Structural Analysis) version 3.5.8. Interfragment charge transfer analysis performed using Multiwfn version 3.8 (dev).

Synthesis

HMAT-BNCz ($C_{73}H_{74}BN_3$, M_w = 1004.2 g mol^{-1}): a dry 50 mL Schlenk flask was charged with BNCz-Br (66 mg, 0.092 mmol, 1 equiv.), HMAT-BPin (45 mg, 0.092 mmol, 1 equiv.), Pd(PPh$_3$)$_4$ (11 mg, 0.0095 mmol, 0.1 equiv.), and K_2CO_3 (139 mg, 1.01 mmol, 11 equiv.), under a positive N_2 atmosphere. In a separate 50 mL round bottom flask, a combination of 6 mL toluene, 2 mL EtOH and 2 mL deionized water were sparged with N_2 for 30 minutes before being transferred *via* cannula to the reaction vessel. The reaction was then heated to 96 °C in an oil bath for 6 hours and completion was assessed by TLC. The reaction was then diluted with 20 mL of deionized water and extracted with toluene (1 × 30 mL) and DCM (2 × 30 mL). The combined organic phase was then evaporated under reduced pressure to give a dark yellow solid. The solid was redissolved in 30 mL DCM and then washed with deionized water (1 × 30 mL) and a brine solution (2 × 30 mL). The organic phase was then dried over anhydrous $MgSO_4$ and evaporated under reduced pressure to give a yellow solid. The crude product was purified by silica column chromatography (gradient column starting at 100% hexanes to 90% hexanes: 10% DCM) and then precipitated out of hexanes to give a bright yellow solid (yield: 73 mg, 79%). ^{1}H NMR (400 MHz, C_6D_6, 298 K): δ_H = 9.53 (d, 2H; $J_{H,H}$ = 1.70 Hz), 8.80 (s, 2H), 8.64 (d, 2H; $J_{H,H}$ = 1.66 Hz), 8.57 (d, 2H; $J_{H,H}$ = 8.87 Hz), 8.44 (d, 2H; $J_{H,H}$ = 1.93 Hz), 8.09 (s, 2H), 7.66 (2 H, dd; $J_{H,H}$ = 8.76, 1.96 Hz), 7.33 (m, 4H), 7.12 (t, 2H; $J_{H,H}$ = 7.63 Hz), 1.74 (s, 12H; ^{i}Pr CH_3), 1.68 (s, 18H; ^{t}Bu CH_3), 1.59 (s, 6H; ^{i}Pr CH_3), 1.46 (s, 18H; ^{t}Bu CH_3). $^{13}C\{^{1}H\}$ NMR (101 MHz, C_6D_6, 298 K): δ_C = 147.2, 145.5, 145.4, 144.9, 142.6, 139.2, 137.2, 132.9, 132.2, 131.1, 130.6, 130.5, 130.2, 129.0, 124.8, 124.4, 124.3, 124.1, 123.8, 123.5, 122.8, 120.9, 117.8, 114.8, 107.7, 36.1, 35.8, 35.3, 35.0, 34.8, 33.5, 33.4, 32.4, 31.9. HRMS (FD): *m/z* calc. for $[C_{73}H_{73}BN_3]^+$ 1002.6012; found 1002.6005; difference 0.7 ppm.

ACR-BNCz ($C_{67}H_{66}BN_3$, M_w = 924.1 g mol^{-1}): a dry 50 mL Schlenk flask was charged with BNCz-Br (67 mg, 0.093 mmol, 1 equiv.), ACR-BPin (38 mg, 0.093 mmol, 1 equiv.), $Pd(PPh_3)_4$ (11 mg, 0.0093 mmol, 0.1 equiv.), and K_2CO_3 (141 mg, 1.02 mmol, 11 equiv.), under a positive N_2 atmosphere. In a separate 50 mL round bottom flask, a combination of 6 mL toluene, 2 mL EtOH and 2 mL deionized water were sparged with N_2 for 30 minutes before being transferred *via* cannula to the reaction vessel. The reaction was then heated to 96 °C in an oil bath for 6 hours and completion was assessed by TLC. The reaction was then diluted with 20 mL of deionized water and extracted with toluene (1 × 30 mL) and DCM (2 × 30 mL). The combined organic phase was then evaporated under reduced pressure to give a dark yellow solid. The solid was redissolved in 30 mL DCM and then washed with deionized water (1 × 30 mL) and a brine solution (2 × 30 mL). The organic phase was then dried over anhydrous $MgSO_4$ and evaporated under reduced pressure to give a yellow solid. The crude product was purified by silica column chromatography (gradient column starting at 96% hexanes: 4% DCM to 70% hexanes: 30% DCM) and then washed with cold hexanes to give a bright yellow solid (yield: 76 mg, 88%). ^{1}H NMR (400 MHz, CD_2Cl_2, 298 K): δ_H = 9.05 (d, 2H; $J_{H,H}$ = 1.60 Hz), 8.52 (s, 2H), 8.47 (d, 2H; $J_{H,H}$ = 1.67 Hz), 8.45 (d, 2H; $J_{H,H}$ = 8.96 Hz), 8.30 (d, 2H; $J_{H,H}$ = 1.88 Hz), 8.18 (s, 2H; $J_{H,H}$ = 8.26 Hz), 7.71 (2 H, dd; $J_{H,H}$ = 8.78, 1.99 Hz), 7.58 (d, 2H; $J_{H,H}$ = 8.22 Hz), 7.53 (dd, 2H; $J_{H,H}$ = 9.05, 1.31 Hz), 7.07 (dd, 2H; $J_{H,H}$ = 6.99, 1.35 Hz), 6.98 (dd, 2H; $J_{H,H}$ = 6.99, 0.95 Hz), 6.52 (dd, 2H; $J_{H,H}$ = 8.18, 0.71 Hz), 1.75 (s, 6H; ^{i}Pr CH_3), 1.66 (s, 18H; ^{t}Bu CH_3), 1.54 (s, 18H; ^{t}Bu CH_3). $^{13}C\{^{1}H\}$ NMR (101 MHz, CD_2Cl_2, 298 K): δ_C = 145.9, 145.4, 145.2, 145.1, 142.0, 141.9, 141.8, 141.4, 138.6, 132.4, 130.7, 130.6, 130.1, 127.5, 126.8, 125.7, 125, 124.0, 122.5, 121.9, 121.3, 121.1, 117.9, 114.7, 114.6, 107.3, 36.4, 35.5, 35.1, 32.3, 31.9, 31.5. HRMS (FD): *m/z* calc. for $[C_{67}H_{65}BN_3]^+$ 922.5386; found 922.5411; difference 2.5 ppm.

Conflicts of interest

The authors declare no conflict of interest.

Data availability

The supporting data has been provided as part of the supplementary information (SI). Supplementary information: Fig. S1–S26, Tables S1–S9 and further experimental details. See DOI: https://doi.org/10.1039/d5tc04366b.

CCDC 2505730 and 2505731 contain the supplementary crystallographic data for this paper.[47]

Acknowledgements

The authors thank the Natural Sciences and Engineering Research Council of Canada (NSERC) for financial support of this work. MJD and RH are grateful for NSERC Graduate Scholarships, and ZMH is grateful for a Killam Accelerator Research Fellowship from the University of British Columbia. The authors also thank Dr Brian Patrick for his assistance with X-ray diffraction analysis, Sydney Mikulin for her assistance with density functional theory calculations, and Elvie Beaumont for her assistance with designing the TOC graphic.

References

1 H. Uoyama, K. Goushi, K. Shizu, H. Nomura and C. Adachi, *Nature*, 2012, **492**, 234–238.
2 X. Wu, B.-K. Su, D.-G. Chen, D. Liu, C.-C. Wu, Z.-X. Huang, T.-C. Lin, C.-H. Wu, M. Zhu, E. Y. Li, W.-Y. Hung, W. Zhu and P.-T. Chou, *Nat. Photonics*, 2021, **15**, 780–786.
3 H.-J. Cheon, S.-J. Woo, S.-H. Baek, J.-H. Lee and Y.-H. Kim, *Adv. Mater.*, 2022, **34**, 2207416.
4 S. Madayanad Suresh, L. Zhang, D. Hall, C. Si, G. Ricci, T. Matulaitis, A. M. Z. Slawin, S. Warriner, Y. Olivier, I. D. W. Samuel and E. Zysman-Colman, *Angew. Chem., Int. Ed.*, 2023, **62**, e202215522.
5 Y. Tang, Y. Liu, W. Ning, L. Zhan, J. Ding, M. Yu, H. Liu, Y. Gao, G. Xie and C. Yang, *J. Mater. Chem. C*, 2022, **10**, 4637–4645.
6 X. Yang, X. Xu and G. Zhou, *J. Mater. Chem. C*, 2015, **3**, 913–944.
7 Z. Xie, C. Cao, Y. Zou, X. Cao, C. Zhou, J. He, C.-S. Lee and C. Yang, *Adv. Funct. Mater.*, 2022, **32**, 2112881.
8 P. E. Burrows, G. Gu, V. Bulovic, Z. Shen, S. R. Forrest and M. E. Thompson, *IEEE Trans. Electron Devices*, 1997, **44**, 1188–1203.
9 N. Aizawa, Y. Harabuchi, S. Maeda and Y.-J. Pu, *Nat. Commun.*, 2020, **11**, 3909.
10 C. M. Marian, *Annu. Rev. Phys. Chem.*, 2021, **72**, 617–640.
11 X. Cai and S.-J. Su, *Adv. Funct. Mater.*, 2018, **28**, 1802558.
12 D. Zhang and L. Duan, *Nat. Photonics*, 2021, **15**, 173–174.
13 Y. Im, M. Kim, Y. J. Cho, J.-A. Seo, K. S. Yook and J. Y. Lee, *Chem. Mater.*, 2017, **29**, 1946–1963.
14 Z. Yang, Z. Mao, Z. Xie, Y. Zhang, S. Liu, J. Zhao, J. Xu, Z. Chi and M. P. Aldred, *Chem. Soc. Rev.*, 2017, **46**, 915–1016.
15 X.-K. Chen, Y. Tsuchiya, Y. Ishikawa, C. Zhong, C. Adachi and J.-L. Brédas, *Adv. Mater.*, 2017, **29**, 1702767.
16 S. Weissenseel, N. A. Drigo, L. G. Kudriashova, M. Schmid, T. Morgenstern, K.-H. Lin, A. Prlj, C. Corminboeuf, A. Sperlich, W. Brütting, M. K. Nazeeruddin and V. Dyakonov, *J. Phys. Chem. C*, 2019, **123**, 27778–27784.

17 T. Hatakeyama, K. Shiren, K. Nakajima, S. Nomura, S. Nakatsuka, K. Kinoshita, J. Ni, Y. Ono and T. Ikuta, *Adv. Mater.*, 2016, **28**, 2777–2781.

18 J.-M. Jin, C. Shi, W.-C. Chen and Y. Huo, *Chem. Commun.*, 2025, **61**, 10731–10746.

19 J. Han, Z. Huang, X. Lv, J. Miao, Y. Qiu, X. Cao and C. Yang, *Adv. Opt. Mater.*, 2022, **10**, 2102092.

20 X. Lv, J. Miao, M. Liu, Q. Peng, C. Zhong, Y. Hu, X. Cao, H. Wu, Y. Yang, C. Zhou, J. Ma, Y. Zou and C. Yang, *Angew. Chem., Int. Ed.*, 2022, **61**, e202201588.

21 S. A. Elgadi, S. Mikulin and Z. M. Hudson, *Adv. Opt. Mater.*, 2025, **13**, 2500683.

22 H. J. Kim and T. Yasuda, *Adv. Opt. Mater.*, 2022, **10**, 2201714.

23 S. A. Elgadi, D. M. Mayder, R. Hojo and Z. M. Hudson, *Adv. Opt. Mater.*, 2023, **11**, 2202754.

24 S. Wu, W. Li, K. Yoshida, D. Hall, S. Madayanad Suresh, T. Sayner, J. Gong, D. Beljonne, Y. Olivier, I. D. W. Samuel and E. Zysman-Colman, *ACS Appl. Mater. Interfaces*, 2022, **14**, 22341–22352.

25 Z. Huang, H. Xie, J. Miao, Y. Wei, Y. Zou, T. Hua, X. Cao and C. Yang, *J. Am. Chem. Soc.*, 2023, **145**, 12550–12560.

26 G. Chen, J. Wang, W.-C. Chen, Y. Gong, N. Zhuang, H. Liang, L. Xing, Y. Liu, S. Ji, H.-L. Zhang, Z. Zhao, Y. Huo and B. Z. Tang, *Adv. Funct. Mater.*, 2023, **33**, 2211893.

27 Y. Xu, C. Li, Z. Li, Q. Wang, X. Cai, J. Wei and Y. Wang, *Angew. Chem., Int. Ed.*, 2020, **59**, 17442–17446.

28 Q. Wu, J. Li, D. Liu, Y. Mei, B. Liu, J. Wang, M. Xu and Y. Li, *Dyes Pigm.*, 2023, **217**, 111421.

29 Y. Liu, X. Xiao, Z. Huang, D. Yang, D. Ma, J. Liu, B. Lei, Z. Bin and J. You, *Angew. Chem., Int. Ed.*, 2022, **61**, e202210210.

30 T. J. Penfold, E. Gindensperger, C. Daniel and C. M. Marian, *Chem. Rev.*, 2018, **118**, 6975–7025.

31 Y. Xu, Z. Cheng, Z. Li, B. Liang, J. Wang, J. Wei, Z. Zhang and Y. Wang, *Adv. Opt. Mater.*, 2020, **8**, 1902142.

32 Y. Qu, Y. Xu, T. Huang, X. Song, K. Ye and Y. Wang, *Angew. Chem., Int. Ed.*, 2025, **64**, e202506201.

33 S. Luo, J. Wang, N. Li, X.-F. Song, X. Wan, K. Li and C. Yang, *Angew. Chem.*, 2023, **135**, e202310943.

34 T. Huang, Y. Xu, Y. Qu, X. Lu, K. Ye, X. Zhuang and Y. Wang, *Adv. Mater.*, 2025, **37**, 2503383.

35 S. Li, Z. Yang, Y. Xie, L. Hua, S. Ying, Y. Liu, Z. Ren and S. Yan, *Chem. Sci.*, 2024, **15**, 18335–18346.

36 R. Hojo, K. Bergmann, S. A. Elgadi, D. M. Mayder, M. A. Emmanuel, M. S. Oderinde and Z. M. Hudson, *J. Am. Chem. Soc.*, 2023, **145**, 18366–18381.

37 E. R. Sauvé, D. M. Mayder, S. Kamal, M. S. Oderinde and Z. M. Hudson, *Chem. Sci.*, 2022, **13**, 2296–2302.

38 R. Hojo, D. M. Mayder and Z. M. Hudson, *J. Mater. Chem. C*, 2022, **10**, 13871–13877.

39 A. M. Polgar, S. H. Huang and Z. M. Hudson, *Polym. Chem.*, 2022, **13**, 3892–3903.

40 D. M. Mayder, C. M. Tonge, G. D. Nguyen, M. V. Tran, G. Tom, G. H. Darwish, R. Gupta, K. Lix, S. Kamal, W. R. Algar, S. A. Burke and Z. M. Hudson, *J. Am. Chem. Soc.*, 2021, **143**, 16976–16992.

41 N. R. Paisley, S. V. Halldorson, M. V. Tran, R. Gupta, S. Kamal, W. R. Algar and Z. M. Hudson, *Angew. Chem., Int. Ed.*, 2021, **60**, 18630–18638.

42 R. Hojo, D. M. Mayder and Z. M. Hudson, *J. Mater. Chem. C*, 2021, **9**, 14342–14350.

43 F.-Y. Hao, Y.-Z. Shi, K. Wang, X.-C. Fan, L. Wu, J. Ye, C.-J. Zheng, Y.-Q. Li, X.-M. Ou and X.-H. Zhang, *J. Mater. Chem. C*, 2020, **8**, 10416–10421.

44 N. Mataga, H. Chosrowjan and S. Taniguchi, *J. Photochem. Photobiol. C Photochem. Rev.*, 2005, **6**, 37–79.

45 J. Wiefermann, J. M. Kaminski, E. Pankert, D. Hertel, K. Meerholz, C. M. Marian and T. J. J. Müller, *ChemPhotoChem*, 2023, **7**, e202200265.

46 F. J. Avila Ferrer, J. Cerezo, E. Stendardo, R. Improta and F. Santoro, *J. Chem. Theory Comput.*, 2013, **9**, 2072–2082.

47 (*a*) CCDC 2505730: Experimental Crystal Structure Determination, 2026, DOI: 10.5517/ccdc.csd.cc2q3f09; (*b*) CCDC 2505731: Experimental Crystal Structure Determination, 2026, DOI: 10.5517/ccdc.csd.cc2q3f1b.